

# Transport Effects on Capacitance-Frequency Analysis for Defect Characterization in Organic Photovoltaic Devices

Liang Xu, Jian Wang, and Julia W. P. Hsu\*

*Department of Materials Science and Engineering, The University of Texas at Dallas,  
800 West Campbell Road, Richardson, Texas 75080, USA*

(Received 24 August 2016; revised manuscript received 16 November 2016; published 28 December 2016)

Using capacitance-frequency ( $C$ - $f$ ) analysis to characterize the density-of-states (DOS) distribution of defects has been well established for inorganic thin-film photovoltaic devices. While  $C$ - $f$  analysis has also been applied to bulk-heterojunction (BHJ) organic photovoltaic (OPV) devices, we show that the low carrier mobility in the BHJ material can severely alter the  $C$ - $f$  behaviors and lead to misinterpretations. Because of the complicated nature of disorders in organic materials, artifacts from an erroneous  $C$ - $f$  analysis are difficult to identify. Here we compare drift-diffusion simulations with experiments to reveal situations when the validity of  $C$ - $f$  analysis for defect characterization breaks down. When a flat-band region is present in the low-mobility active layer, the capacitive response cannot follow the electrical modulation and behaves as if the active layer is a dielectric at frequencies higher than the characteristic frequency determined by carrier mobility and thickness. The transition produces a fictitious shallow defect when defect analysis is applied. Even in fully depleted devices, the defect distributions derived from  $C$ - $f$  analysis can appear at spuriously deeper energies if the mobility is too low. Through simulations, we determine the ranges of mobility and thickness for which the  $C$ - $f$  analysis can effectively yield credible defect DOS information. Insight from this study also sheds light on transport limitation when using capacitance spectroscopy for defect characterization in general.

DOI: [10.1103/PhysRevApplied.6.064020](https://doi.org/10.1103/PhysRevApplied.6.064020)

## I. INTRODUCTION

Defect states are well known to plague organic photovoltaic (OPV) devices by increasing charge recombination, deteriorating charge transport, and increasing exciton annihilation [1–4]. Accurate defect-state characterization is, thus, critical in OPV device research. Several techniques, such as capacitance-frequency ( $C$ - $f$ ) analysis [5], deep-level transient spectroscopy [6], thermally stimulated current [7], and current density–voltage ( $J$ - $V$ ) modeling [8] have been used to identify defect distribution in OPV devices. It is well known that the presence of defects modifies the frequency-dependent capacitance behavior [9–11]. The  $C$ - $f$  analysis was first applied to investigate the defect-state energy and distribution in inorganic thin-film photovoltaic devices by Walter *et al.* [12] and Hegedus *et al.* [13] and recently adapted to characterize defect states in OPV devices [5,14–19] and perovskite photovoltaic devices [20,21]. Another approach is to perform capacitance-voltage ( $C$ - $V$ ) measurements under a few frequencies [11,22], but this method can roughly estimate only the total defect-state density and not defect energetics obtained in  $C$ - $f$  analysis.

In order for  $C$ - $f$  analysis to probe the capture or emission process of defect states with characteristic frequencies

corresponding to their energy positions within the band gap, the capacitive response of the mobile carriers must be frequency independent over the entire measurement frequency range (typically 0.1 Hz–1 MHz). Generally, this assumption is valid for inorganic materials, which usually have the mobility higher than  $1 \text{ cm}^2 \text{ V}^{-1} \text{ s}^{-1}$  [23,24]. However, for the bulk-heterojunction- (BHJ) type OPV devices where charge transport heavily relies on hopping processes, their effective charge mobility is usually lower by orders of magnitude ( $10^{-3}$ – $10^{-7} \text{ cm}^2 \text{ V}^{-1} \text{ s}^{-1}$ ), especially at low temperatures [25–27]. Under such circumstances, conducting carriers become unresponsive at high frequencies, and the frequency dependence of capacitance is severely altered. As a result, artifacts can arise from applying the same defect reconstruction from  $C$ - $f$  data as in inorganic studies without careful examination. Moreover, due to the complicated nature of disorders in organic materials [28], spurious results due to transport are hard to be distinguished from real defects and, thus, misinterpreted. In the literature, several studies do not consider the effect of low mobility in BHJ OPV devices with published results susceptible to transport-related artifacts [14–19].

In this study, we elucidate the transport effect on  $C$ - $f$  analysis by performing experimental studies of OPV devices with varying thickness and mobility and comparing the results with drift-diffusion simulations. An inevitable transition from depletion capacitance to geometric capacitance is demonstrated in devices with a flat-band region,

\*Corresponding author.  
jwhsu@utdallas.edu

which correspondingly introduces a fictitious shallow level into the derived defect density of states (DOS). Even in fully depleted devices, the low mobility leads to more reduction of capacitive response from real defects at higher frequencies, therefore, a shift of the defect distribution to spuriously deeper energies which do not accurately reflect the real defect position. Finally, we establish a zone of confidence in terms of mobility and thickness ranges where accurate defect characterization by  $C$ - $f$  analysis can be achieved. Insight from this study also sheds light on the effect of transport on performing capacitance-based defect characterization on devices and materials in general beyond OPV devices, especially at low temperatures.

## II. BACKGROUND

Using  $C$ - $f$  analysis to determine the defect DOS distribution in photovoltaics was initially established by Walter *et al.* [12] and Hegedus *et al.* [13]. This method consists of calculating the derivative of the junction capacitance with respect to the angular frequency of the ac modulation, which is corrected by a factor accounting for the band bending and the drop of the modulation signal over the space-charge region of the junction. Figure 1(a) demonstrates the band diagram of a fully depleted semiconductor simulating the active layer of a BHJ OPV device in the dark at equilibrium (zero voltage bias). A band bending develops across the active layer as the Fermi level ( $E_f$ ) of the electrodes aligns with the  $E_f$  of the semiconductor. In this study, we consider hole traps with peak energy at  $E_0$  between the midgap and valence-band edge ( $E_v$ , or highest occupied molecular orbital in organic semiconductors), since OPV devices are typically  $p$ -type doped [7,29–31]. The occupation of such a defect level at a given spatial position is determined by its energy with respect to the local  $E_f$  as shown in Fig. 1(a), with  $M$  denoting the position where  $E_0$  equals  $E_f$ . Because of the presence of the band bending, all the states spatially to the right of  $M$  (above  $E_f$ ) are occupied by holes (filled hole traps indicated by the solid line), while all the states to the left of  $M$  (below  $E_f$ ) are not occupied by holes (empty hole traps indicated by the dashed line). In the capacitance measurement, a small perturbation of the ac voltage effectively modulates the occupation of the defect states at  $M$ , i.e., capture and emission of holes from these states, which, in turn, contributes to the junction capacitance.

For the defects acting as hole traps, the characteristic time  $\tau$  of thermal emission from a defect state residing within the band gap to the valence band is given by [13]

$$\tau = \gamma^{-1} \exp\left(\frac{\Delta E}{k_B T}\right), \quad (1)$$

where  $k_B T$  is the thermal energy,  $\gamma$  is the attempt-to-escape frequency ( $\gamma = v_{th} \sigma_p N_v$ , where  $v_{th}$  is the thermal velocity,

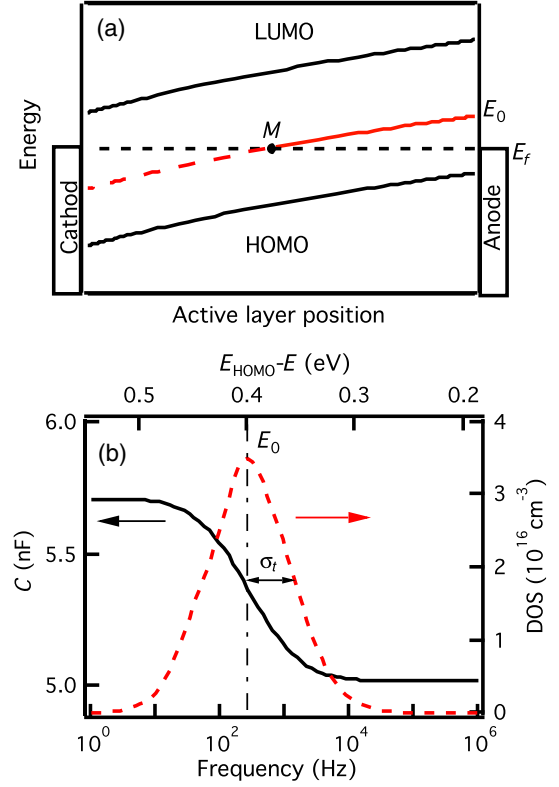


FIG. 1. (a) Schematic band diagram of a  $p$ -doped device in the dark at zero bias voltage. The crossing point between the Fermi level  $E_f$  and the defect energy  $E_0$ ,  $M$ , within the depletion zone marks the position of the occupancy change. (b)  $C$  vs  $f$  in the dark at zero bias (black solid line) of the device shown in (a) and the corresponding defect DOS distribution (red dashed line) derived from the  $C$ - $f$  spectrum using Eq. (3), which has a Gaussian distribution with a peak energy at  $E_0$  and a disorder width  $\sigma_t$ .

$\sigma_p$  is the hole capture cross section, and  $N_v$  is the valence-band effective density of states), and  $\Delta E$  is the difference between the defect energy level and the valence-band edge ( $\Delta E = E_v - E_0 > 0$ ).  $1/\tau$  sets the maximal frequency at which the defect states are still able to respond to the ac modulation and contribute to the junction capacitance. The condition  $\omega\tau = 1$  ( $\omega = 2\pi f$  is the angular frequency of the ac modulation, while  $f$  is the measurement frequency) occurs at  $\omega_E$ , which corresponds to a demarcation energy  $E_\omega$ :

$$E_\omega = \Delta E = k_B T \ln\left(\frac{\gamma}{\omega_E}\right). \quad (2)$$

$E_\omega$  defines the energy level (relative to  $E_v$ ) of defect states that can respond when subjected to ac modulation with angular frequencies lower than  $\omega_E$ . Thus, each capacitance transition corresponds to a distinct defect state with demarcation energy corresponding to the transition frequency according to Eq. (2).

To probe the entire defect spectrum, the frequency of the ac modulation is varied from 1 to  $10^6$  Hz, and Eq. (2) is applied to obtain all demarcation energies associated with different defect states. In this approach, it is assumed that the frequency dependence of the junction capacitance is determined only by the defect emission rate, so the capacitance spectrum reflects the defect-energy landscape, with high frequencies corresponding to energy levels near the valence band and sweeping towards midgap as the frequency decreases. The defect DOS distribution is further taken to be proportional to the derivative of the capacitance with respect to the frequency as [12]

$$\text{DOS}(E_\omega) = -\frac{V_{\text{FB}}\omega}{qdk_B T} \frac{dC(\omega)}{d\omega}, \quad (3)$$

where  $q$  is the magnitude of elementary charge,  $d$  the depletion region width, and  $V_{\text{FB}}$  the flat-band potential. For a defect with a peak DOS at  $E_0$ , Fig. 1(b) shows its  $C$ - $f$  behavior (black solid line) and corresponding defect DOS distribution derived from the  $C$ - $f$  spectrum (red dashed line), which is typically analyzed by a Gaussian function:

$$\text{DOS}(E) = \frac{N_t}{\sqrt{2\pi}\sigma_t} \exp\left[-\frac{(E_0 - E)^2}{2\sigma_t^2}\right], \quad (4)$$

where  $\sigma_t$  is the disorder width, and  $N_t$  is the total defect density.

### III. EXPERIMENTAL DETAILS

#### A. Device fabrication

All chemicals are purchased from Fisher Scientific and used as received, and all processing is performed in a  $\text{N}_2$  glovebox (Innovative Technology) unless otherwise noted.

Inverted BHJ devices are fabricated on patterned indium tin oxide (ITO; Xinyan,  $15 \Omega/\text{square}$ ). A ZnO electron-transport layer (approximately 30 nm) is spin coated at 2000 rpm in air using a solution having 0.5 M of zinc acetate dihydrate and 0.5 M of monoethanolamine dissolved in a 2-methoxyethanol and then pyrolyzed at  $300^\circ\text{C}$  for 10 min in air. For the BHJ active layer, poly(3-hexylthiophene) (P3HT; RMI-001E, Rieke Metals, Inc.) and [6,6]-phenyl C61-butyric acid methyl ester ( $\text{PC}_{61}\text{BM}$ ; Solenne BV) are dissolved in anhydrous chlorobenzene (CB; Sigma-Aldrich) at varying concentrations from 8 to 32 mg/mL and spin coated at varying spin speeds between 700 and 1500 rpm to obtain different thicknesses. All films are annealed at  $170^\circ\text{C}$  for 10 min in  $\text{N}_2$  after deposition, and a 7-nm  $\text{MoO}_3$  hole transport layer (HTL) and a 100-nm Ag electrode are thermally evaporated (Angstrom Engineering) to complete the devices, with a junction area of  $0.11 \text{ cm}^2$  each.

For the conventional fullerene-based devices, 30 nm of poly(3,4-ethylenedioxythiophene):poly(styrenesulfonate) (PEDOT:PSS) (Heraeus Clevios AI 4083) is spin coated

onto precleaned ITO substrates followed by  $140^\circ\text{C}$  annealing in  $\text{N}_2$  for 10 min to form the HTL. P3HT and [6,6]-phenyl C71-butyric acid methyl ester ( $\text{PC}_{71}\text{BM}$ ; Solenne BV) with a total concentration of 25 mg/mL are dissolved overnight in CB solution with varying P3HT concentrations between 1 and 20 wt%. Active-layer thicknesses between 60 and 70 nm are spin cast at 1500–4000 rpm (to keep film thickness constant for all P3HT concentrations) for 60 s. All active layers are annealed at  $70^\circ\text{C}$  in  $\text{N}_2$  for 10 min after deposition. Finally, Ca (7 nm) and Al (100 nm) are thermally evaporated to complete the devices. For the hole-only devices,  $\text{MoO}_3$  (7 nm) and Ag (100 nm) are thermally evaporated following the active layer.

#### B. Device characterization

The  $J$ - $V$  measurements are performed in a  $\text{N}_2$ -filled glovebox under AM1.5G  $100 \text{ mW}/\text{cm}^2$  illumination from a class AAA solar simulator (Abet Technologies) using a low-noise sourcemeter (2635 A, Keithley) controlled by a LabVIEW program. The solar simulator intensity is set using a National Institute of Standards and Technology-traceable calibrated photodiode (Abet RR\_227KG5). A 2.5-mm-diameter aperture is placed in front of each device to rigorously define the illumination area of  $0.049 \text{ cm}^2$ .

Impedance spectroscopy (IS) measurements used for extracting the capacitance value are carried out in an O-ring sealed sample holder containing  $\text{N}_2$  at room temperature using a Zahner IM6 electrochemical workstation. They are performed in the dark with an ac bias (20 mV) modulating between 1 Hz and 1 MHz.

### IV. EXPERIMENTAL RESULTS AND DISCUSSION

#### A. Effect of the flat-band region on defect characterization

It is well documented that the active layer of OPV devices is typically a moderately  $p$ -doped material with a background carrier density from  $5 \times 10^{15}$  to  $7 \times 10^{16} \text{ cm}^{-3}$  [7,29–31]. The  $p$ -type doping is typically unintentional and caused by oxygen, moisture, and/or impurities acting as  $p$ -type dopants [7,31,32]. Meanwhile, 200–300 nm is established as the optimal active-layer thickness in several BHJ systems [33–37]. However, due to partial screening of the built-in electrical field by background carriers, the depletion region of the active layer is usually limited to  $< 150 \text{ nm}$ , leaving a non-negligible flat-band (field-free) region [30,31,35,38].

P3HT, the most well-studied polymer in OPV devices, is known to be  $p$ -type doped with a background carrier density of  $5 \times 10^{15}$  to  $5 \times 10^{16} \text{ cm}^{-3}$  [5,7,39]. While the optimal thickness for P3HT: $\text{PC}_{61}\text{BM}$  OPV devices is approximately 200 nm [33], devices with thickness varying between 100 [38] and 800 nm [40] have been studied. To understand how the flat-band region impacts defect

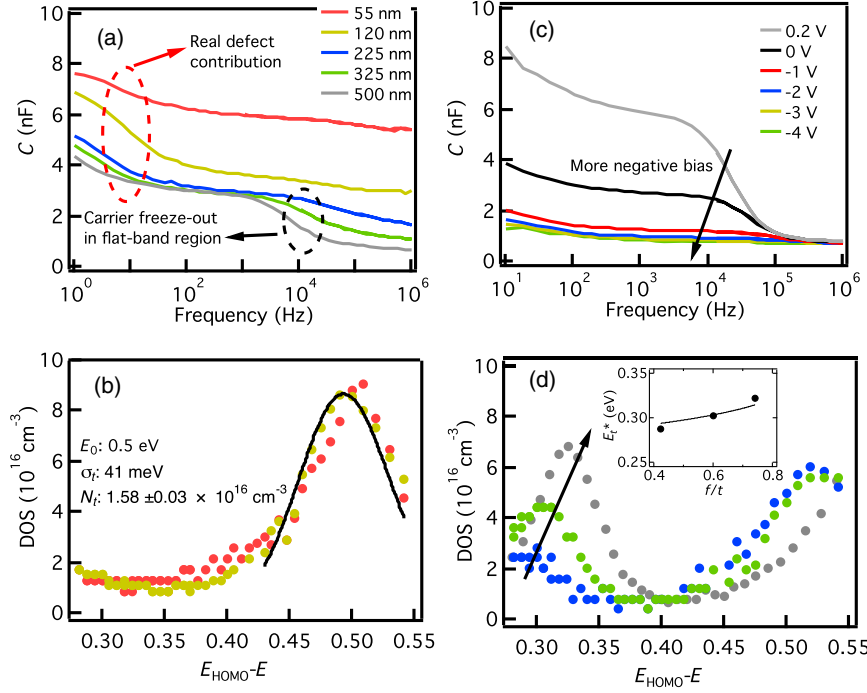


FIG. 2. (a)  $C$  vs  $f$  in the dark at zero bias for inverted P3HT:PC<sub>61</sub>BM devices with different active-layer thicknesses: 55 nm (red), 120 nm (dark yellow), 225 nm (blue), 325 nm (green), and 500 nm (gray). Defect DOS derived from  $C$ - $f$  analysis for 55- and 120-nm devices. The solid line in (b) shows the Gaussian fit of the defect DOS according to Eq. (4); the corresponding fitting parameters are shown as the inset. (c)  $C$  vs  $f$  for a 500-nm-thick P3HT:PC<sub>61</sub>BM device under different biases: 0.2 V (gray), 0 V (black), -1 V (red), -2 V (blue), -3 V (dark yellow), and -4 V (green). (d) Defect DOS derived from  $C$ - $f$  analysis for 225-, 325-, and 500-nm devices. All color schemes used in (b) and (d) are the same as in (a). The inset of (d) depicts the spurious shallow-defect peak position  $E_t^*$  vs  $f/t$  for the three thicker devices with a fit according to Eq. (9).

characterization, we investigate the  $C$ - $f$  behavior (in the dark and at zero bias) in inverted ITO/ZnO/P3HT:PC<sub>61</sub>BM/MoO<sub>3</sub>/Ag devices with active-layer thickness varying between 55 and 500 nm [41] [Fig. 2(a), and see Fig. S1 and Table S1 in the Supplemental Material [42] for  $J$ - $V$  characteristics]. The capacitance value is extracted from the IS measurements [43]

$$C = \frac{1}{\omega} \left[ \frac{Z'' - \omega L}{(Z' - R_s)^2 + (Z'' - \omega L)^2} \right], \quad (5)$$

where  $Z'$  and  $Z''$  are the real (in-phase) and imaginary (out-of-phase) components of the measured impedance,

respectively,  $R_s$  is the series resistance, and  $L$  is the parasitic inductance. Notice that within the common frequency range of IS measurement ( $10^{-1}$ – $10^6$  Hz), while  $L$  can usually be ignored,  $R_s$  should always be measured (the value of  $Z'$  at 1 MHz is used for  $R_s$  in our study, as shown in the Supplemental Material [42] Table S1) and included in Eq. (5) to obtain an accurate capacitance value [43,44]. Capacitance at high frequency decreases severely without the  $R_s$  correction, deviating from its real value (see the Supplemental Material [42] Fig. S2).

All devices with varying thickness show a continuous decrease in capacitance with increasing frequency below 100 Hz [red dashed ellipse in Fig. 2(a)], indicating the existence of deep defect states. In the frequency range

TABLE I. Material parameters used for drift-diffusion simulation.

Parameters	Symbol (unit)	BHJ device	Fullerene-based device
Electron affinity	$E_A$ (eV)		3.7 [45]
Conduction-band and valance-band effective density of states	$N_{n,p}$ (cm <sup>-3</sup> )		$1 \times 10^{20}$ [29]
Anode work function	$E_{WF,A}$ (eV)	Aligned with active-layer Fermi level	
Cathode work function	$E_{WF,C}$ (eV)		4.0 [45]
Bimolecular recombination coefficient	$k$ (cm <sup>3</sup> s <sup>-1</sup> )		$2 \times 10^{-12}$ [39]
Electron mobility	$\mu_e$ (cm <sup>2</sup> V <sup>-1</sup> s <sup>-1</sup> )		$2 \times 10^{-3}$ [39]
Background hole concentration	$p$ (cm <sup>-3</sup> )		$5.8 \times 10^{15}$
Relative permittivity $\epsilon$	$\epsilon$	3.6	4.5 [46]
Effective band gap	$E_g$ (eV)	1.1 [29]	1.45 [39]
Electron-hole capture cross section	$\sigma_{n,p}$ (cm <sup>2</sup> )		$1 \times 10^{-17}$ <sup>a</sup>
Maximum of the defect distribution	$E_{t,0}$ (eV)		0.26 <sup>b</sup>
Disorder of the defect distribution	$\sigma_t$ (meV)		22 <sup>b</sup>
Total defect density	$N_t$ (cm <sup>-3</sup> )		$6.02 \times 10^{15}$ <sup>b</sup>

<sup>a</sup>The electron-hole capture cross section is reported to be within in the range of  $1 \times 10^{-18}$ – $1 \times 10^{-16}$  cm<sup>-2</sup> [18,47].

<sup>b</sup>Using the adjusted experimental value of the 20% P3HT device. See the Supplemental Material [42] Fig. S9 for details.



between 100 Hz and 1 kHz, all  $C$ - $f$  curves exhibit a plateau, which decreases monotonically with increasing active-layer thickness and saturates for thicknesses greater than 225 nm. The saturated capacitance plateau value reflects the maximum depletion-region width, which is approximately 130 nm with  $C = 2.7$  nF at 1 kHz and  $z = 3.6\epsilon_0$  (see the Supplemental Material [42] Table S1) for these devices. Hence, while the two thinnest devices are completely depleted, there must exist a flat-band region in the active layer for the three thicker devices. In these devices, there is an additional step decrease of capacitance [black dashed ellipse in Fig. 2(a)] at higher frequencies ( $>10$  kHz), which is associated with the transition from junction capacitance ( $C_d$ ) to geometric capacitance ( $C_g$ ) with a characteristic frequency  $\omega_t$ .  $C_d$  originates from the charges accumulated at the two boundaries of the depletion region, which have to transport throughout the quasineutral flat-band region to contribute to the capacitance signal, while  $C_g$  stems from the dielectric response of the material, i.e., the local movement of charges with net charges at the two electrodes. Such capacitance transition is due to carrier freeze-out in the quasineutral flat-band region with poor conductivity, and details can be found in the Supplemental Material [42] Fig. S3 as well as previous publications [24,48].

Figure 2(b) demonstrates the defect DOS distributions of the fully depleted 55- and 120-nm devices derived from the  $C$ - $f$  analysis using Eq. (3). Very similar DOS distributions located at approximately 0.5 eV are observed in these two devices. When fitted with Eq. (4),  $E_0 = 0.5$  eV, a  $\sigma_t = 41$  meV, and a  $N_t = 1.58 \pm 0.03 \times 10^{16}$  cm $^{-3}$  are obtained [black line in Fig. 2(b)], which are in good agreement with previous published results [5].

To further verify that the step decrease of capacitances at higher frequencies ( $>10$  kHz) in the (225–500)-nm devices is due to the existence of a flat-band region in the active layer, we perform the  $C$ - $f$  measurement under different dc voltage biases. Figure 2(c) illustrates the  $C$ - $f$  behavior of a 500-nm P3HT:PC $_{61}$ BM device under bias from 0.2 to  $-4$  V. With increasing negative bias, the depletion width approaches the entire active-layer thickness. As a result,  $C_d$  becomes closer to  $C_g$ , and, thus, the capacitance transition gradually disappears. Figure 2(c) unambiguously shows that the capacitance value above  $10^5$  Hz for all biases is  $C_g$ , while  $C_d$  can be measured only below  $10^4$  Hz (also see the Supplemental Material [42] Fig. S4); correspondingly, the transition between  $10^4$  and  $10^5$  Hz is not due to defects. However, if one were to apply Eq. (4) to the entire  $C$ - $f$  spectra, a fictitious defect corresponding to the  $C_d$ -to- $C_g$  transition at high frequency [black dashed ellipse in Fig. 2(a)] appears at approximately 0.3 eV in the (225–500)-nm devices [Fig. 2(d)]. Additionally, the peak energy of the fictitious defect distribution ( $E_t^*$ ) shifts to higher energy corresponding to lower characteristic frequency with increasing active-layer thickness. The dependence of  $E_t^*$  on the

fraction of flat-band region in the active layer is further examined:

$$E_t^* = k_B T \ln \left( \frac{\gamma \epsilon}{q p \mu_h (1 - \frac{f}{t})} \right), \quad (6)$$

where  $\epsilon$  is the dielectric constant of the active layer,  $p$  is the hole carrier concentration,  $\mu_h$  is the hole mobility,  $f$  is the width of flat-band region, and  $t$  is the total thickness of the active layer ( $t = d + f$ ). See the Supplemental Material [42] Eq. (S3) and the related discussion for a detailed derivation. As shown in the inset of Fig. 2(d), fitting  $E_t^*$  for devices with different  $f/t$  yields a reasonable  $\mu_h = 7 \times 10^{-5}$  cm $^2$  V $^{-1}$  s $^{-1}$  [49] given that  $p$  is determined to be  $5.8 \times 10^{15}$  cm $^{-3}$  (Supplemental Material [42] Fig. S4),  $\epsilon$  is set to be  $3.6\epsilon_0$  (Supplemental Material [42], Table S1), and a  $\gamma$  of  $10^{10}$  s $^{-1}$  is adopted. While an accurate measurement of  $\gamma$  is difficult in BHJ OPV devices (we discuss this in more detail later in this paper), values ranging from  $10^7$  to  $10^{10}$  s $^{-1}$  are generally used or reported in the literature [16,18,50]. Such a variation of  $\gamma$  results only in an uncertainty of  $\pm 90$  meV in the *absolute* energy position of the defects according to Eq. (2) without affecting the DOS distribution. Since we are not studying the accurate determination of defect-energy positions in this paper, but instead to elucidate the effect of poor transport, a physically reasonable  $\gamma$  value of  $10^{10}$  s $^{-1}$  is adequate for this purpose.

Next, we use the SCAPS 1D drift-diffusion simulator developed by the group of Professor Burgelman at the University of Gent [51–53] to simulate the  $\mu_h$  effect on the  $C_d$ -to- $C_g$  transition and the corresponding artifact in the defect characterization by  $C$ - $f$  analysis (simulation parameters are detailed in Table I). No actual defect is assumed in the simulations. Based on a 225-nm device with a flat-band region of approximately 90 nm [Supplemental Material [42] Fig. S5(a)] and varying  $\mu_h$  from  $10^{-3}$  to  $10^{-6}$  cm $^2$  V $^{-1}$  s $^{-1}$ , a range typically found in BHJ materials [25], the simulations all show a capacitance transition [Fig. 3(a)], which translates to a fictitious shallow-defect state [Supplemental Material [42] Fig. S5(b)]. The peak energy of these fictitious defects ( $E_t^*$ ) is plotted as a function of  $\mu_h$  [Fig. 3(b)], from which a logarithmic decrease of  $E_t^*$  with increasing  $\mu_h$  is observed. These results indicate that by applying defect characterization using  $C$ - $f$  analysis to the OPV system with a flat-band region, the capacitance transition from  $C_d$  to  $C_g$  and, hence, fictitious shallow-defect states, is unavoidable.

While the existence of shallow defects as band-tail states are well known in OPV devices [54,55], based on this study, we caution that misinterpretations might be present in the published literature, and we emphasize that care should always be taken when interpreting a high-frequency capacitance decrease in the  $C$ - $f$  analysis of OPV devices [14–19]. Performing  $C$ - $f$  measurements under varying

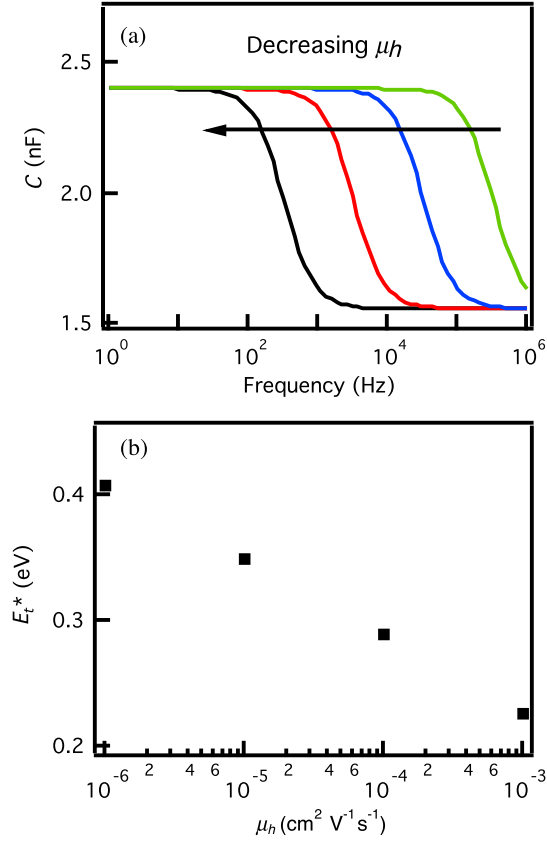


FIG. 3. The simulated fictitious shallow-defect position  $E_t^*$  for a 225-nm device with  $p = 5.8 \times 10^{15} \text{ cm}^{-3}$  and hole mobility varying from  $10^{-6} \text{ cm}^2 \text{V}^{-1} \text{s}^{-1}$  to  $10^{-3} \text{ cm}^2 \text{V}^{-1} \text{s}^{-1}$ . Inset:  $C$  vs  $f$  for different mobilities: black ( $10^{-6} \text{ cm}^2 \text{V}^{-1} \text{s}^{-1}$ ), red ( $10^{-5} \text{ cm}^2 \text{V}^{-1} \text{s}^{-1}$ ), blue ( $10^{-4} \text{ cm}^2 \text{V}^{-1} \text{s}^{-1}$ ), and green ( $10^{-3} \text{ cm}^2 \text{V}^{-1} \text{s}^{-1}$ ).

biases, as shown in Fig. 2(c), provides an effective approach to probe the existence of the flat-band region, and, therefore, it is recommended to ensure that  $C_d$  is correctly measured before extracting the defect DOS.

### B. Effect of low hole mobility in fully depleted devices

Recent high-performance OPV devices mostly use relatively thin (approximately 100 nm) and, therefore, fully depleted active layers to ensure good charge collections [56,57]. To further assess the effect of hole mobility in fully depleted devices, which does not manifest the fictitious shallow defect due to the  $C_d$ -to- $C_g$  transition (Fig. 2), we investigate the PC<sub>71</sub>BM-based OPV devices with small amounts of P3HT [46] (see Supplemental Material [42] Fig. S6 and Table S2 for  $J$ - $V$  characteristics). As shown in Fig. 4(a), in all P3HT concentrations, the capacitance decreases as the frequency increases; additionally, with decreasing P3HT concentration, the capacitance decrease shifts to lower frequency. The capacitance values shown are

normalized to the value at 1 MHz, i.e., the  $C_g$ , to remove the contribution from thickness variation [see Supplemental Material [42] Fig. S7(a) for the non-normalized capacitance data]. As a result, the corresponding defect-state distributions derived from the  $C$ - $f$  data (normalized to peak value for clear comparison) show a large variation in energy: with decreasing P3HT concentration, the defect DOS distribution shifts towards the midgap [Fig. 4(b); see Supplemental Material [42] Fig. S7(b) for DOS before normalization]. To understand this phenomenon, we first measure the hole mobility (Supplemental Material [42] Fig. S8) on hole-only devices (ITO/PEDOT:PSS/active layer/MoO<sub>3</sub>/Ag) following the space-charge-limited current modeling [58]. We find that the hole mobility is strongly dependent on the donor concentration in the fullerene-based devices (Supplemental Material [42] Table S3), consistent with the published literature [59–61]. While the  $\mu_h$  of the 1 wt % P3HT device ( $7.0 \times 10^{-7} \text{ cm}^2 \text{V}^{-1} \text{s}^{-1}$ ) is close to the value of pristine PC<sub>71</sub>BM [59], it is 2 orders of magnitude higher in the 20 wt % P3HT device ( $3.0 \times 10^{-5} \text{ cm}^2 \text{V}^{-1} \text{s}^{-1}$ ).

While the capacitance of a dielectric is due to its polarization by the applied field, the defect-induced capacitance involves charge transport. In response to the electrical modulation, the displacement current is generated from charges emitted from defects and results in an effect on the junction capacitance. Therefore, an effective  $C$ - $f$  defect characterization is realized only when the average charge-transit time in the device  $\tau_d$  is much shorter than  $1/\omega$  ( $\tau_d \ll 1/\omega$ ). However, given a  $\mu_h$  of the order of  $10^{-6} \text{ cm}^2 \text{V}^{-1} \text{s}^{-1}$ ,  $\tau_d$  is of the order  $10^{-5} \text{ s}$  in a device approximately 100 nm thick, and, thus,  $\tau_d \ll 1/\omega$  is no longer satisfied at frequencies higher than 10 kHz. Consequently, the contribution to junction capacitance from charges emitted from defect states is reduced in the way that the capacitance decreases more at higher frequency.

To quantify this observation, we simulate the mobility effect on the defect characterization in devices with varying  $\mu_h$  ( $7.0 \times 10^{-7} - 3.0 \times 10^{-5} \text{ cm}^2 \text{V}^{-1} \text{s}^{-1}$ ). See Table I for other parameters in detail. We introduce a defect DOS with a constant Gaussian distribution into the simulation at  $E_{t,0} = 0.26 \text{ eV}$  (see Supplemental Material [42] Fig. S9 for details). With the same input defect DOS, the simulations reproduce the trend in  $C$ - $f$  behavior with the capacitance decrease shifting to lower frequency [Fig. 4(c)] and the corresponding defect energy shifting towards deeper energy with decreasing  $\mu_h$  [Fig. 4(d)]. Therefore, the shifts of the extracted defect distributions in Fig. 4(b) are artifacts from the  $C$ - $f$  analysis arising from the limited transport of holes. Given that all devices have the same materials, P3HT and PC<sub>71</sub>BM, the defect is expected to have the same energy level in all devices. Indeed, our previous work shows that the energetics measured from the low-energy quantum-efficiency spectroscopy is the same in all devices with varying P3HT concentration [46]. The experimental studies together with the simulation results indicate that

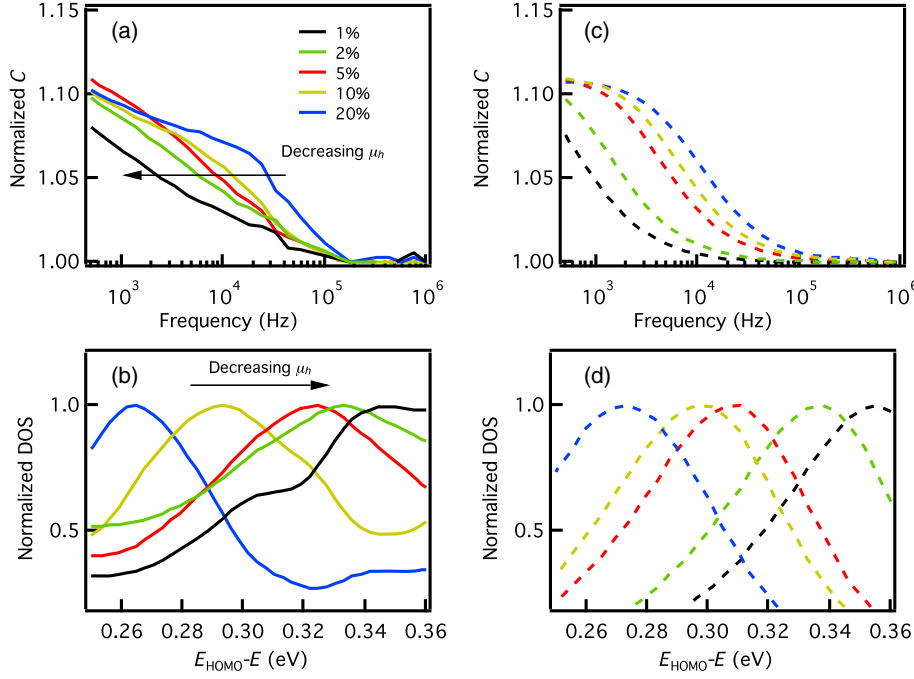


FIG. 4. (a)  $C$  vs  $f$  of the fullerene-based OPV devices with different P3HT concentration: 1 wt % (black), 2 wt % (green), 5 wt % (red), 10 wt % (dark yellow), and 20 wt % (blue). All results are normalized to the value at 1 MHz. The arrow indicates the shift of  $C$ - $f$  with decreasing  $\mu_h$  (P3HT concentration). (b) Defect DOS distributions extracted from (a). All results are normalized to their peak value to emphasize the energy position change. The arrow indicates the shift to deeper position in the device with decreasing  $\mu_h$  (P3HT concentration). (c) Normalized  $C$ - $f$  simulated for the fullerene-based OPV devices with different  $\mu_h$  values that correspond to P3HT concentrations. (d) Corresponding simulated defect DOS distributions (normalized). All color schemes used in (b), (c), and (d) are the same as in (a).

even in fully depleted thin devices, the low mobility can introduce artifacts and spurious measurements of defect-energy position. Note that for the thicker devices shown in Fig. 3, the real defect position shifts to  $>0.5$  eV [Fig. 2(d)], which is a consequence of the same limited charge-transport effect discussed here.

Figure 5 depicts simulation results that show the combined effects of hole mobility and active-layer thickness on the validity of defect characterization using the  $C$ - $f$  method. The  $\mu_h$  value (y axis) is varied within the range ( $1 \times 10^{-7}$ – $1 \times 10^{-3}$   $\text{cm}^2 \text{V}^{-1} \text{s}^{-1}$ ) [25], while the thickness  $t$  (x axis, 50–130 nm) is set within the range of a fully depleted active layer [based on the result of different thickness devices in Fig. 2(a)], which also covers the range most relevant to high-performance OPV devices [56,57]. The color indicates the energy position shift,  $\Delta E_t = E_{t,s} - E_{t,0}$ , where  $E_{t,s}$  is the simulation output of the energy peak position of the defect DOS distribution. The white line demonstrates a boundary below which there is no artifact; i.e., the  $C$ - $f$  analysis can be applied to characterize defect distributions with accuracy (the green area). With decreasing  $\mu_h$  (moving upwards) and increasing  $t$  (moving rightwards), a larger  $\Delta E_t$ , i.e., a more severe artifact, is observed. The failure of the  $C$ - $f$  analysis in this region is due to the long charge-transit time set by the combination of the charge mobility and device thickness. While a  $\mu_h$  in the order of  $10^{-5}$   $\text{cm}^2 \text{V}^{-1} \text{s}^{-1}$  still ensures accurate defect characterizations by  $C$ - $f$  analysis in devices with an active layer thinner than 60 nm, generally,  $\mu_h \sim 10^{-4}$   $\text{cm}^2 \text{V}^{-1} \text{s}^{-1}$  is the threshold for using  $C$ - $f$  analysis in practical devices with reasonably good performance (approximately 100 nm).

The transport-limited  $C$ - $f$  behavior, as we address above, further sheds light on the application of other capacitance-based techniques for defect characterization. Deep-level transient spectroscopy (DLTS) is commonly used to study defects in semiconductors by measuring a capacitance transient associated with the defect thermal emission [50,62,63]. In the case of low-mobility materials and devices, the frequency used for measuring capacitance should always be carefully evaluated to ensure that the defect contribution is accurately captured by the capacitance measured. More importantly, low-temperature measurements are often used in capacitance-based defect characterization (including both  $C$ - $f$  analysis and DLTS) for obtaining the defect activation energy and the attempt-to-escape frequency [18,62–64]. However, in the BHJ OPV devices, mobility is reported to decrease by orders of magnitude at low temperatures [26,27]. Even for the optimized P3HT:PCBM BHJ OPV device, which is among the highest-mobility OPV devices, the mobility drops to  $10^{-6}$ – $10^{-7}$   $\text{cm}^2 \text{V}^{-1} \text{s}^{-1}$  below 100 K [26]. With such low mobility, the capacitance behavior is severely altered (Fig. 5). As a result, the defect activation energy and/or attempt-to-escape frequency obtained from an Arrhenius plot can be erroneous. Therefore, to accurately extract these quantities in BHJ OPV devices, a better modeling, which takes into account the temperature dependence of mobility, is desired.

## V. CONCLUSION

In summary, we examine the accuracy of defect characterization by  $C$ - $f$  analysis in OPV devices by comparing experimental data with drift-diffusion simulations. Since



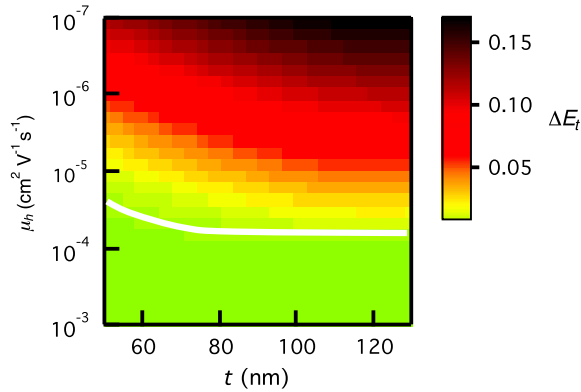


FIG. 5. Simulation results of devices with varying hole mobility (y axis) in logarithmic scale and active-layer thickness (x axis). The color indicates the energy position shift of the defect DOS distributions between the output and input of the simulations. The white line demonstrates a boundary below which there is no artifact.

the  $C$ - $f$  analysis probes the capacitance contribution from the charges emitted from defect states, the  $C$ - $f$  analysis is only accurate when all the emitted charges can efficiently respond to the electrical modulation at the measurement frequency (0.1 Hz–1 MHz). The low mobility in organic materials raises concerns when applying the  $C$ - $f$  technique for defect characterization. In an OPV device having a flat-band region in the active layer, a fictitious shallow-defect state is found to be inevitable due to the limited charge transport in the flat-band region that results in the capacitance transition from the depletion to the geometric capacitance within the measurement frequency range. Even in devices with a fully depleted active layer, low mobilities lead to an apparent shift in the derived defect-energy position because the capacitance contribution from defects is more reduced at higher frequencies. The simulations indicate that for a device of approximately 100 nm, using the  $C$ - $f$  analysis to extract defect DOS distributions produces true defect distribution when the hole mobility exceeds  $10^{-4} \text{ cm}^2 \text{ V}^{-1} \text{ s}^{-1}$ . Thus, special caution should be taken when using  $C$ - $f$  analysis for defect characterization in OPV devices. The findings from this study indicate that there can also be a transport limit on the validity of defect characterization techniques based on capacitance spectroscopy when studying materials and devices in general beyond OPV devices, especially at low temperatures.

## ACKNOWLEDGMENTS

We thank Professor William Vandenberghe for his valuable suggestions as well as his reading of this manuscript. This work is sponsored by the National Science Foundation Grant No. DMR-1305893. J. W. P. H. acknowledges the support from the Texas Instruments Distinguished Chair in Nanoelectronics.

- [1] O. V. Mikhnenko, M. Kuik, J. Lin, N. van der Kaap, T. Q. Nguyen, and P. W. M. Blom, Trap-limited exciton diffusion in organic semiconductors, *Adv. Mater.* **26**, 1912 (2014).
- [2] R. A. Street, J. E. Northrup, and B. S. Krusor, Radiation induced recombination centers in organic solar cells, *Phys. Rev. B* **85**, 205211 (2012).
- [3] R. A. Street, A. Krakaris, and S. R. Cowan, Recombination through different types of localized states in organic solar cells, *Adv. Funct. Mater.* **22**, 4608 (2012).
- [4] Z. Liang, A. Nardes, D. Wang, J. J. Berry, and B. A. Gregg, Defect engineering in  $\Pi$ -conjugated polymers, *Chem. Mater.* **21**, 4914 (2009).
- [5] P. P. Boix, G. Garcia-Belmonte, U. Muñecas, M. Neophytou, C. Waldauf, and R. Pacios, Determination of gap defect states in organic bulk heterojunction solar cells from capacitance measurements, *Appl. Phys. Lett.* **95**, 233302 (2009).
- [6] S. Neugebauer, J. Rauh, C. Deibel, and V. Dyakonov, Investigation of electronic trap states in organic photovoltaic materials by current-based deep level transient spectroscopy, *Appl. Phys. Lett.* **100**, 263304 (2012).
- [7] J. Schafferhans, A. Baumann, A. Wagenpfahl, C. Deibel, and V. Dyakonov, Oxygen doping of P3HT: PCBM blends: Influence on trap states, charge carrier mobility and solar cell performance, *Org. Electron.* **11**, 1693 (2010).
- [8] C.-Y. Nam, D. Su, and C. T. Black, High-performance air-processed polymer-fullerene bulk heterojunction solar cells, *Adv. Funct. Mater.* **19**, 3552 (2009).
- [9] C. T. Sah and V. G. K. Reddi, Frequency dependence of the reverse-biased capacitance of gold-doped silicon  $p^+n$  junctions, *IEEE Trans. Electron Devices* **11**, 345 (1964).
- [10] E. P. EerNisse, Accurate capacitance calculations for  $p$ - $n$  junctions containing traps, *Appl. Phys. Lett.* **18**, 183 (1971).
- [11] L. C. Kimerling, Influence of deep traps on the measurement of free-carrier distributions in semiconductors by junction capacitance techniques, *J. Appl. Phys.* **45**, 1839 (1974).
- [12] T. Walter, R. Herberholz, C. Müller, and H. W. Schock, Determination of defect distributions from admittance measurements and application to Cu(In,Ga)Se<sub>2</sub> based heterojunctions, *J. Appl. Phys.* **80**, 4411 (1996).
- [13] S. S. Hegedus and E. A. Fagen, Midgap states in  $a$ -Si:H and  $a$ -SiGe:H  $p$ - $i$ - $n$  solar cells and Schottky junctions by capacitance techniques, *J. Appl. Phys.* **71**, 5941 (1992).
- [14] T. Muntasir and S. Chaudhary, Understanding defect distributions in polythiophenes via comparison of regioregular and regiorandom species, *J. Appl. Phys.* **118**, 205504 (2015).
- [15] T. Muntasir and S. Chaudhary, Defects in solution-processed dithienylsilole-based small-molecule photovoltaic thin-films, *J. Appl. Phys.* **119**, 025501 (2016).
- [16] S. Khelifi, K. Decock, J. Lauwaert, H. Vrielinck, D. Spoltore, F. Piersimoni, J. Manca, A. Belghachi, and M. Burgelman, Investigation of defects by admittance spectroscopy measurements in poly (3-hexylthiophene):(6,6)-phenyl C61-butyric acid methyl ester organic solar cells degraded under air exposure, *J. Appl. Phys.* **110**, 094509 (2011).
- [17] D. Spoltore, W. D. Oosterbaan, S. Khelifi, J. N. Clifford, A. Viterisi, E. Palomares, M. Burgelman, L. Lutsen,



- D. Vanderzande, and J. Manca, Effect of polymer crystallinity in P3HT:PCBM solar cells on band gap trap states and apparent recombination order, *Adv. Energy Mater.* **3**, 466 (2013).
- [18] J. A. Carr, M. Elshobaki, and S. Chaudhary, Deep defects and the attempt to escape frequency in organic photovoltaic materials, *Appl. Phys. Lett.* **107**, 203302 (2015).
- [19] B. Ecker, J. C. Nolasco, J. Pallarés, L. F. Marsal, J. Posdorfer, J. Parisi, and E. von Hauff, Degradation effects related to the hole transport layer in organic solar cells, *Adv. Funct. Mater.* **21**, 2705 (2011).
- [20] M. Samiee, S. Konduri, B. Ganapathy, R. Kottokkaran, H. A. Abbas, A. Kitahara, P. Joshi, L. Zhang, M. Noack, and V. Dalal, Defect density and dielectric constant in perovskite solar cells, *Appl. Phys. Lett.* **105**, 153502 (2014).
- [21] Y. Shao, Z. Xiao, C. Bi, Y. Yuan, and J. Huang, Origin and elimination of photocurrent hysteresis by fullerene passivation in  $\text{CH}_3\text{NH}_3\text{PbI}_3$  planar heterojunction solar cells, *Nat. Commun.* **5**, 5784 (2014).
- [22] V. V. Brus, C. M. Proctor, N. A. Ran, and T.-Q. Nguyen, Capacitance spectroscopy for quantifying recombination losses in nonfullerene small-molecule bulk heterojunction solar cells, *Adv. Energy Mater.* **6**, 1502250 (2016).
- [23] E. A. Schiff, R. I. Devlen, H. T. Grahn, J. Tauc, and S. Guha, Picosecond electron drift mobility measurements in hydrogenated amorphous silicon, *Appl. Phys. Lett.* **54**, 1911 (1989).
- [24] J. Lee, J. D. Cohen, and W. N. Shafarman, The determination of carrier mobilities in CIGS photovoltaic devices using high-frequency admittance measurements, *Thin Solid Films* **480–481**, 336 (2005).
- [25] D. Bartesaghi, I. D. C. Pérez, J. Kniepert, S. Roland, M. Turbiez, D. Neher, and L. J. A. Koster, Competition between recombination and extraction of free charges determines the fill factor of organic solar cell, *Nat. Commun.* **6**, 7083 (2015).
- [26] A. Baumann, J. Lorrman, D. Rauh, C. Deibel, and V. Dyakonov, A new approach for probing the mobility and lifetime of photogenerated charge carriers in organic solar cells under real operating conditions, *Adv. Mater.* **24**, 4381 (2012).
- [27] B. Ebenhoch, S. A. J. Thomson, K. Genevicius, G. Juska, and I. D. W. Samuel, Charge carrier mobility of the organic photovoltaic materials PTB7 and PC71BM and its influence on device performance, *Org. Electron.* **22**, 62 (2015).
- [28] L. G. Kaake, P. F. Barbara, and X. Y. Zhu, Intrinsic charge trapping in organic and polymeric semiconductors: A physical chemistry perspective, *J. Phys. Chem. Lett.* **1**, 628 (2010).
- [29] T. Kirchartz, W. Gong, S. A. Hawks, T. Agostinelli, R. C. I. MacKenzie, Y. Yang, and J. Nelson, Sensitivity of the Mott-Schottky analysis in organic solar cells, *J. Phys. Chem. C* **116**, 7672 (2012).
- [30] F. Deledalle, T. Kirchartz, M. S. Vezie, M. Campoy-Quiles, P. Shakya Tuladhar, J. Nelson, and J. R. Durrant, Understanding the Effect of Unintentional Doping on Transport Optimization and Analysis in Efficient Organic Bulk-Heterojunction Solar Cells, *Phys. Rev. X* **5**, 011032 (2015).
- [31] J. Wang, L. Xu, Y.-J. Lee, M. De Anda Villa, A. V. Malko, and J. W. P. Hsu, Effects of contact-induced doping on the behaviors of organic photovoltaic devices, *Nano Lett.* **15**, 7627 (2015).
- [32] M. Nyman, S. Dahlström, O. J. Sandberg, and R. Österbacka, Unintentional bulk doping of polymer-fullerene blends from a thin interfacial layer of  $\text{MoO}_3$ , *Adv. Energy Mater.* **6**, 1600670 (2016).
- [33] G. Dennler, M. C. Scharber, and C. J. Brabec, Polymer-fullerene bulk-heterojunction solar cells, *Adv. Mater.* **21**, 1323 (2009).
- [34] Y. Liu, J. Zhao, Z. Li, C. Mu, W. Ma, H. Hu, K. Jiang, H. Lin, H. Ade, and H. Yan, Aggregation and morphology control enables multiple cases of high-efficiency polymer solar cells, *Nat. Commun.* **5**, 1 (2014).
- [35] G. F. A. Dibb, M.-A. Muth, T. Kirchartz, S. Engmann, H. Hoppe, G. Gobsch, M. Thelakkat, N. Blouin, S. Tierney, M. Carrasco-Orozco, J. R. Durrant, and J. Nelson, Influence of doping on charge carrier collection in normal and inverted geometry polymer:fullerene solar cells, *Sci. Rep.* **3**, 3335 (2013).
- [36] S. C. Price, A. C. Stuart, L. Yang, H. Zhou, and W. You, Fluorine substituted conjugated polymer of medium band gap yields 7% efficiency in polymer-fullerene solar cells, *J. Am. Chem. Soc.* **133**, 4625 (2011).
- [37] J. Peet, L. Wen, P. Byrne, S. Rodman, K. Forberich, Y. Shao, N. Drolet, R. Gaudiana, G. Dennler, and D. Waller, Bulk heterojunction solar cells with thick active layers and high fill factors enabled by a bithiophene-co-thiazolothiazole push-pull copolymer, *Appl. Phys. Lett.* **98**, 043301 (2011).
- [38] T. Kirchartz, T. Agostinelli, M. Campoy-Quiles, W. Gong, and J. Nelson, Understanding the thickness-dependent performance of organic bulk heterojunction solar cells: The influence of mobility, lifetime, and space charge, *J. Phys. Chem. Lett.* **3**, 3470 (2012).
- [39] Y.-J. Lee, B. L. Adkison, L. Xu, A. A. Kramer, and J. W. P. Hsu, Comparison of conventional and inverted organic photovoltaic devices with controlled illumination area and extraction layers, *Sol. Energy Mater. Sol. Cells* **144**, 592 (2016).
- [40] J. G. Tait, U. W. Paetzold, D. Cheyns, M. Turbiez, P. Heremans, and B. P. Rand, Interfacial depletion regions: Beyond the space charge limit in thick bulk heterojunctions, *ACS Appl. Mater. Interfaces* **8**, 2211 (2016).
- [41] L. Xu, Y.-J. Lee, and J. W. P. Hsu, Charge collection in bulk heterojunction organic photovoltaic devices: An impedance spectroscopy study, *Appl. Phys. Lett.* **105**, 123904 (2014).
- [42] See Supplemental Material at <http://link.aps.org/supplemental/10.1103/PhysRevApplied.6.064020> for  $J$ - $V$  curves and device parameters of OPV devices with different thicknesses and P3HT concentrations,  $C$ - $f$  curve with and without series resistance correction, detailed discussion on  $C_d$ -to- $C_g$  transition, dopant density obtained from  $C$ - $V$  curves at different frequencies, drift-diffusion simulations of defect DOS for different mobilities, non-normalized  $C$ - $f$  and DOS data for different P3HT concentration devices,  $J$ - $V$  curves of hole-only devices and the fitting parameters, DOS derived from the  $C$ - $f$  curve for the 20% P3HT OPV device, and the simulation result.

- [43] V. V. Brus, On impedance spectroscopy analysis of nonideal heterojunctions, *Semicond. Sci. Technol.* **27**, 035024 (2012).
- [44] J. A. Carr and S. Chaudhary, On accurate capacitance characterization of organic photovoltaic cells, *Appl. Phys. Lett.* **100**, 213902 (2012).
- [45] B. W. Larson, J. B. Whitaker, X.-B. Wang, A. A. Popov, G. Rumbles, N. Kopidakis, S. H. Strauss, and O. V. Boltalina, Electron affinity of phenyl-C 61-butyric acid methyl ester (PCBM), *J. Phys. Chem. C* **117**, 14958 (2013).
- [46] L. Xu, J. Wang, M. de A. Villa, T. B. Daunis, Y.-J. Lee, A. V. Malko, and J. W. P. Hsu, Quantitative analyses of competing photocurrent generation mechanisms in fullerene-based organic photovoltaics, *J. Phys. Chem. C* **120**, 16470 (2016).
- [47] R. C. I. MacKenzie, C. G. Shuttle, M. L. Chabinye, and J. Nelson, Extracting microscopic device parameters from transient photocurrent measurements of P3HT:PCBM solar cells, *Adv. Energy Mater.* **2**, 662 (2012).
- [48] J. V. Li, A. M. Nardes, Z. Liang, S. E. Shaheen, B. A. Gregg, and D. H. Levi, Simultaneous measurement of carrier density and mobility of organic semiconductors using capacitance techniques, *Org. Electron.* **12**, 1879 (2011).
- [49] J. A. Bartelt, D. Lam, T. M. Burke, S. M. Sweetnam, and M. D. McGehee, Charge-carrier mobility requirements for bulk heterojunction solar cells with high fill factor and external quantum efficiency >90%, *Adv. Energy Mater.* **5**, 1500577 (2015).
- [50] A. J. Campbell, D. Bradley, E. Werner, and W. Brütting, Deep level transient spectroscopy (DLTS) of a poly (p-phenylene vinylene) Schottky diode, *Synth. Met.* **111–112**, 273 (2000).
- [51] M. Burgelman, P. Nollet, and S. Degraeve, Modelling polycrystalline semiconductor solar cells, *Thin Solid Films* **361**, 527 (2000).
- [52] A. Niemegeers and M. Burgelman, in *Proceedings of 25th IEEE Photovoltaic Specialists Conference, Washington, DC* (IEEE, New York, 1996), p. 901.
- [53] M. Burgelman, K. Decock, S. Khelifi, and A. Abass, Advanced electrical simulation of thin film solar cells, *Thin Solid Films* **535**, 296 (2013).
- [54] R. A. Street, Electronic structure and properties of organic bulk-heterojunction interfaces, *Adv. Mater.* **28**, 3814 (2016).
- [55] T. Kirchartz, B. E. Pieters, J. Kirkpatrick, U. Rau, and J. Nelson, Recombination via tail states in polythiophene: fullerene solar cells, *Phys. Rev. B* **83**, 115209 (2011).
- [56] Z. He, B. Xiao, F. Liu, H. Wu, Y. Yang, S. Xiao, C. Wang, T. P. Russell, and Y. Cao, Single-junction polymer solar cells with high efficiency and photovoltage, *Nat. Photonics* **9**, 174 (2015).
- [57] T. Ma, K. Jiang, S. Chen, H. Hu, H. Lin, Z. Li, J. Zhao, Y. Liu, Y.-M. Chang, C.-C. Hsiao, and H. Yan, Efficient low-bandgap polymer solar cells with high open-circuit voltage and good stability, *Adv. Energy Mater.* **5**, 1501282 (2015).
- [58] J. C. Blakesley, F. A. Castro, W. Kylberg, G. F. A. Dibb, C. Arantes, R. Valaski, M. Cremona, J. S. Kim, and J.-S. Kim, Towards reliable charge-mobility benchmark measurements for organic semiconductors, *Org. Electron.* **15**, 1263 (2014).
- [59] B. Yang, Z. Xiao, and J. Huang, Polymer aggregation correlated transition from Schottky-junction to bulk heterojunction organic solar cells, *Appl. Phys. Lett.* **104**, 143304 (2014).
- [60] M. Zhang, H. Wang, H. Tian, Y. Geng, and C. W. Tang, Bulk heterojunction photovoltaic cells with low donor concentration, *Adv. Mater.* **23**, 4960 (2011).
- [61] C. M. Proctor, A. S. Kher, J. A. Love, Y. Huang, A. Sharenko, G. C. Bazan, and T.-Q. Nguyen, Understanding charge transport in molecular blend films in terms of structural order and connectivity of conductive pathways, *Adv. Energy Mater.* **6**, 1502285 (2016).
- [62] D. V. Lang, Deep-level transient spectroscopy: A new method to characterize traps in semiconductors, *J. Appl. Phys.* **45**, 3023 (1974).
- [63] Y. S. Yang, S. H. Kim, J.-I. Lee, H. Y. Chu, L.-M. Do, H. Lee, J. Oh, T. Zyung, M. K. Ryu, and M. S. Jang, Deep-level defect characteristics in pentacene organic thin films, *Appl. Phys. Lett.* **80**, 1595 (2002).
- [64] J. V. Li, S. W. Johnston, Y. Yan, and D. H. Levi, Measuring temperature-dependent activation energy in thermally activated processes: A 2D Arrhenius plot method, *Rev. Sci. Instrum.* **81**, 033910 (2010).